LAWRENCE
LIVERMORE
NATIONAL
LABORATORY

LLNL-JRNL-771753

In situ observation of material flow in composite media under shock compression

D. B. Bober, J. Lind, M. Kumar

April 11, 2019

Physical Review Materials

Disclaimer

In situ observation of material flow in composite media under shock compression

David B. Bober [1*], Jonathan Lind [1], Mukul Kumar [1]

[1] Lawrence Livermore National Laboratory, Livermore, CA 94550, United States

*E-mail: bober1@llnl.gov

Abstract

When a shock wave enters a heterogeneous material, local differences in density and compressibility drive pressure and velocity gradients which can be nearly as sharp as the incident shock. Subsequent momentum equilibration is comparatively slow, relying on shock reverberation, particle collisions and shear flow. The latter phenomenon depends on constitutive behavior that is often poorly known and so the process can be problematic to simulate. This is compounded by the fact that conventional diagnostics, such as velocimetry, blend the response of both phases and provide only a homogenized comparison for modeling efforts. For these reasons, we have collected spatially resolved and phase-specific measurements on a model particulate composite using in situ synchrotron-based radiography. This revealed the post-shock internal motion, including nanosecond resolution measurement of the metal particles' trajectories and snapshots of the flow field within the polymer. Comparing this data to analytical and numerical predictions allowed the polymer's shear response to be inferred. The resulting constitutive model was then used in conjunction with direct numerical simulations to demonstrate the physical origins of the observed bulk composite response.

Keywords: Shock Compression; Heterogeneous material; Composite; Multiphase Flow

Introduction

Strong impulsive loading from an explosive detonation, intense radiation, or high-speed impact occurs in fields ranging from ballistics to oil extraction and astrophysics. These events launch high amplitude compression waves that travel faster than the ambient speed of sound in the host material, i.e. shock waves. The region of material overrun by the shock is transformed into a high-pressure state, with accompanying physical and chemical changes, such as the conversion of graphite into diamond [1]. These transformations in turn effect the shape of the compression wave front, imprinting it with information about the material. For example, the volume collapse associated with certain phase transformations manifests as a splitting of the shock into two waves traveling at different speeds [2]. Characteristic wave signatures have also been recognized for many other phenomena, like detonation [3] and plasticity [4], making shock wave profiles a valuable diagnostic for studying material behavior. However, not all phenomena are equally amenable to this sort of detection, such as a chemical reaction that results in little volume change and therefore leaves only minor evidence in the material's velocity history [5]. Alternately, multiple phenomena can interact to leave strong signatures on the wave profile, but in a way that obscures their individual origins.

Heterogeneous materials present a case in which the shock wave profiles are sensitive to multiple phenomena that can be difficult to deconvolve. Consider the case of particulate composites in which hard/dense inclusions are randomly dispersed inside a soft/light matrix, like saturated soil and polymer bonded explosives. The shock waves moving through these mixtures show features that are not seen for the individual constituents. For example, Figure 1 shows a recently published example for the shock wave profile of a polymer filled with 5 vol% W powder, along with that of the unfilled polymer [6]. Something about the composite nature of the

polymer-W blend causes a pronounced rounding of the velocity history which is not seen in the pure polymer, nor would it be in the pure W. Rauls and Ravichandran [7] and Setchell et al. [8] have shown that such temporal spreading of the shock wave is linked to the size of the particles in the composite, with smaller particles producing a shorter rise time. Anderson et al. [9] have shown that the viscosity of the matrix material also influences the time needed for these materials to reach equilibrium. The commonality is that the interaction of the phases is central to shaping the wave. In addition, the phase fraction [6-8] and relative mechanical properties play an important role. What remains unsolved is the quantitative link between these distinct phenomena and the observed shock response.

We believe that this deficit stems from the near exclusive use of 1D velocimetry, which has two crucial shortcomings. First, it yields only a spatially averaged measure of the distinct phases. This obscures the different paths that they take toward equilibrium and their interactions with each other. As was just discussed, these interactions are thought to be a key part of the physics. Second, the mechanisms in question are expected to produce very similar effects on the observed wave profiles, and so are a difficult to definitively identify. As Barker [10] showed in 1971, a wave reverberation phenomenon can be mimicked by a viscoelastic model given the right set of 'material' properties. This problem would become more tractable were it possible to reverse the typical inference direction by starting with in-situ observations. In the ideal case, the state of both phases would be measured at high spatiotemporal resolution, revealing the underlying physical mechanisms and leading to accurate wave profile predictions.

Toward this goal, we collected high speed radiographic images of a model particulate composite undergoing shock compression. The composite consisted of W spheres arranged inside a polymer matrix in such a way as to allow their motion to be tracked at nanosecond

resolution. Along with observation of the polymer flow field, this data makes it possible to answer basic questions, like whether the polymer acts more like a plastic solid or a viscous fluid. This information feeds into the material models used in finite element simulations of the bulk composite. The internal states from these calculations illustrate how of the momentum transfer process controls the continuum wave profile.

In the following, we begin by describing how a model material was tailored to the available radiographic capabilities in order to access nanosecond timescales. The momentum transfer between constituents will then be analyzed using a velocity history built from the X-ray images. This measurement is then used to evaluate and parameterize candidate models for the polymer's shear response. Estimating the polymer's shear resistance will be a primary focus because this information is not otherwise available, and it is required for physically grounded predictions of the bulk composite response. Such finite element predictions are then discussed, with the resulting wave profiles compared against recently published experimental observations. The internal states from these calculations will be used to illustrate the balance of the underlying forces. The mechanisms observed will be summarized by a scaling analysis that delineates a regime dominated by the matrix shear properties from one governed by impedance mismatch between the constituents. This hopefully begins to reconcile competing schools of thought for how to understand the shock response of particulate composites.

Materials and Methods

The goal of the first experiment was to measure the acceleration of 20 μm W spheres embedded within a block of polymer subjected to high speed plate impact. This was possible because of the high-speed radiography capability at the Dynamic Compression Sector (35-ID) at the Advanced Photon Source (APS) at Argonne National Laboratory. Sector 35-ID provides state

of the art spatiotemporal resolution not available with more conventional flash X-rays, making it possible to image micron scale objects on a 34 ps timescale [11]. The experimental setup is illustrated in Figure 2 (a), which shows the arrangement of the sample, projectile and X-ray imaging direction. From previous measurements of this composite's continuum shock response, it was hypothesized that the 20 μm particles would reach velocity equilibrium with the polymer on the order of 25 ns [6]. This was much less than the synchrotron bunch and camera inter-frame timing of 153.4 ns and so precluded tracking a single particle with the necessary temporal resolution. This limitation was circumvented by tracking the position of >100 particles, each of whose displacement is a function of the time elapsed since the shock overtook its original position. Given identical particles placed in a staggered array, the time resolution of the reconstructed trajectory was only limited by the spacing of the particles and the shock speed. Their positions were chosen to balance the desire for close spacing along the shock direction against the need for large particle-particle separation, non-overlapping X-ray projections, and edge effect avoidance. The configuration chosen is shown in Figure 2 (b) and resulted in a minimum spacing of 250 μm between nearest neighbors but arranged such that the shock wave would encounter a particle every 3.8 μm. For a wave speed of ~4 km/s, this implies the particle position would be probed every ~1 ns. The particle radii had an estimated standard deviation of ±1 μm.

The goal of the second experiment was to measure the flow field in the same polymer-W composite by introducing tracers like those used in experimental fluid mechanics. In the ideal case, these move with the surrounding fluid but do not affect it. To serve this purpose, very thin (~100 nm) Au films were placed inside the polymer, aligned parallel to the shock plane. Their projected thickness along the X-ray direction was intended to produce high contrast, while their

extreme thinness along the shock direction would lead to negligible mechanical disturbance. To remain visible in the radiographs, these films needed to maintain a single axis of curvature parallel to the X-ray direction. To create such a flow field, three W cylinders were embedded in the polymer, with cylinder axis parallel to the X-ray direction. These had diameters of 12.7, 25.4 and 50.8 μm, each having an estimated uncertainty of ±0.5 μm in diameter. This geometry is shown in Figure 2 (c). In both experimental geometries, the polymer block was supported on the impact side by a 1 mm thick Al buffer plate. Further details of the target fabrication, shock driver and X-ray imaging setup are in the supplemental material (Appendix A).

Results and Discussion

Observation of particle trajectories and surrounding flow field

Everything that follows stems from two series of radiographs that show the motion of a shocked polymer and embedded metal features. The first set of images is concerned with the motion of the 20 μm W spheres, shown as dark spots in Figure 3 (a). The shock front is visible in each frame as a sharp change in x-ray transmission through the polymer, with the less dense unshocked polymer to the right. It moved from left to right at a speed of 3.9 km/s. The black region at the left of each image is the Al buffer, which moves from left to right at 1.4 km/s. Stress continuity requires that this must also be the post-shock material velocity of the polymer in regions not disturbed by the W. The W particles appear as an array of dark spots within the polymer. These also swept left to right following the shock, though their motion is less obvious to the eye. Note that this is a projected X-ray image and so the particles in the 3D array are in fact much farther from their apparent neighbors than it appears; see Figure 2 (b) for orthogonal schematic views. The labeled frame times are relative to when the first image was acquired.

The second series of images focus on the motion of the polymer around included W cylinders, as shown in Figure 3 (b). As before, the shock front can be seen in each frame as the sharp change within the polymer, while the buffer is the dark region on the far left, and the cylinders are viewed in projection as dark circles. By design, the Al buffer moves left to right in the experiment at 1.4 km/s, and the polymer shock speed is also 3.9 km/s. In addition to these now familiar features, Figure 3 (b) also shows 7 dark vertical bands. These are the Au films designed to track the motion of the polymer. To better see the evolution of these tracers, the images in Figure 3 (b) have been translated such that the buffer occupies the same location in each. This provides a view as though the camera was flying along with the buffer and thus removes the rigid body translation for the compressed material. At the moment before the shock arrives at the W cylinders in frame 1, the Au films are all planar and the cylinders are tangent to the 4^{th} one, counting from left to right. After the shock has passed in frames 2-4, the 4^{th} Au film is found to the right of the cylinders. This is because the W cylinders are slow to accelerate and so the faster-moving polymer flows past them, carrying along the Au films. That the Au films do not disturb the hydrodynamics is due to their extreme thinness, being only ~100 nm thick. That this is truly the case can be seen by the fact that the Au moves at the same rate as the polymer/buffer far from the W. The flow around the cylinders can be seen via the curvature in the Au. There is a trailing disturbance to the right of the largest two cylinders, and a less pronounced leading one to their left, akin to stern and bow wakes. The lateral extent of this disturbance is relatively small, on the order of only 1 diameter. This validates the previously ad hoc assumption of independence between the individual wires and spheres. The tracers also show no sign of vortex shedding or turbulence. Interestingly, the tracer material that was initially tangent to the cylinders later shows a disconnect from them. This suggests that slip is

occurring at the polymer-W interface because a no-slip boundary would cause a layer of Au to envelope the W and form a continuous trail. This presumes low Reynold's number flow, the validity of which will be discussed shortly.

The relative motion between W particles is difficult to see in Figure 3 (a), and so quantitative position tracking was applied. Figure 4 (a) shows the displacement of the buffer and each particle from their pre-shock positions as a function of time since shock arrival at each. The buffer serves as a proxy for the undisturbed polymer because they move together. This shows that the particle motion initially lags the buffer/far field polymer motion (1.4 km/s). As more time elapsed, the particles continued to accelerate and eventually moved with a speed matching that of the buffer. To break down this acceleration process further, it is informative to transform reference frames to look at the particle displacements relative to the Al buffer and polymer instead of relative to the laboratory frame. This is shown in Figure 4 (b), where the horizontal axis still represents the time elapsed since each sphere encountered the shock. The initial velocity difference between the W and the polymer is very large, as seen by the initially steep slope in Figure 4 (b). As time passed, the particles accelerated enough that they came to rest relative to the moving polymer, which is shown by the plateau in Figure 4 (b) starting at ~100 ns.

The displacements of the cylinders in Figure 3 (b) can be quantified in the same way, although the time resolution is limited to the inter-frame time of 153.4 ns. This data is plotted in Figure 5, with the reference frame again taken to move with the buffer. This is an x-t diagram where each point has been extracted from the images in Figure 3 (b). The positions of the Au films, as measured far from the cylinders, are also plotted. The position of the buffer is obviously close to stationary because the reference frame is taken from its average velocity. The Au films will be seen to track with the Al buffer, supporting the idea that they simply follow the

polymer without significantly disturbing it. As would be expected for an inertia dominated process, the thinner wires undergo less relative motion than the thicker ones. This can be seen from their differences in motion compared to the Au films. The largest cylinder accelerates so slowly that it is overtaken by three Au films. In other words, the three Au films which were originally to the left of the large cylinder are carried to its right. In comparison, the smallest cylinder was only passed by one Au film, indicating less motion relative to the polymer.

The observations above have been mostly qualitative in nature, using the trajectories to illustrate trends that are hard to glean from the raw images. However, the real value of Figure 4 is that it provides a means to estimate the shear resistance of the polymer. Though this idea dates back at least to Höppler's invention of the falling-ball viscometer, Al'tshuler, Kanel and Chekin [12] were the first to put it into practice for shock compressed condensed matter by electromagnetically recording the velocity history of a wire entrained in water. The wire's trajectory was compared to predictions from Newtonian fluid mechanics and used to estimate the viscosity [12]. Kim [13] later incorporated more of the experiment's dynamic nature into the analysis, followed by further measurements on glycerin by Al'tshuler, Doronin and Kim [14]. Abramson [15] has recently highlighted the importance of accounting for nonmonotonicity in the drag curve. The next section will start along the track established by these previous works before evaluating a non-Newtonian model and re-introducing the polymer flow field as a complimentary diagnostic.

Polymer shear resistance

The observed trajectories of the entrained W spheres can be compared against any model that predicts the polymer-particle force as a function of time. Given such a model, all that needs to be done is to integrate Newton's second law once with respect to time to get velocity and then

again to get position. The more difficult task is predicting the polymer-W force. At short timescales, this force is expected to be dominated by the pressure wave of the incident shock. The actual interaction time for the incident shock and particles is given by

$$\tau_s = \frac{d}{U_s} \qquad \text{Equation 1}$$

where d is the particle diameter, and U_s is the shock speed [16]. Evaluating Equation 1 for the spherical particle diameter of 20 μm and the shock speed of 3.9 km/s gives a time of only ~5 ns. During this brief interval, Figures 4 (a) shows that the spheres reach only a small fraction of their final velocity. This indicates that the incident shock is not the main driver of momentum transfer to the particles. This occurs because of the extreme impedance mismatch between the phases. Subsequent acceleration must be due to a more sustained force, for example fluid drag or shear strength. Unfortunately, not even the qualitative nature of the polymer's shear response is known. One approach is to pick some trial model, determine the range of possible particle trajectories that it predicts for a given parameter set, then check if any of them match the experimental observations.

Newtonian fluid model

The effect of elastic shear in the polymer can be gauged by how the W displaced when all other forces were removed, akin to the interpretation of the unloading portion in other mechanical tests. Such conditions were present when the W came to rest relative to the moving polymer, a period which is shown in Figure 4 starting at ~100 ns. At that time, whatever drag force was previously exerted by the differential flow would vanish and leave only elastic forces. Such elastic forces would tend to reverse the particle displacement, causing a spring-back. In Figure 4 (a) this should appear as an upward curvature in the blue line. Likewise, in figure 4 (b),

elastic rebound would cause the plateau region to take on a negative curvature, meaning that the particles would tend back toward zero displacement in the moving reference frame. Neither trend was observed, and instead the particles remained at rest relative to the surrounding polymer, at least to within the experimental resolution. This indicates that elasticity did not produce measurable deformation in the relevant timeframe. While such recovery could theoretically have occurred later, these slow timescales are neither measurable in these experiments, nor relevant to the phenomena being studied. Therefore, candidate models must only account for the polymer flow stress and can safely ignore elastic shear.

A Newtonian fluid model was selected as an initial guess for the polymer response because it produces an exponentially decaying trajectory with a single unknown material parameter, the dynamic viscosity (μ). Given some range of viscosities, it is possible to compute the drag force on the particle as a function of time. The Clift-Gauvin drag model was selected because it covers the appropriate range of Reynolds number, which is discussed along with the accompanying assumptions in the supplemental material (Appendix B). The trajectory predicted for a viscosity of 8 Pa·s, the best fitting value, is plotted in Figure 6 (a). It is accompanied by trajectories for viscosities that are scaled by 0.5, 0.67, 0.8, 1.25, 1.5 and 2. These additional trajectories are included to give an idea of the sensitivity to viscosity. Two additional trajectories are also plotted in Figure 6 (a) for a viscosity of 8 Pa·s, but assuming particle radii ±1 μm from the mean. This represents the approximate standard deviation within the population of particles in the experiment. Individual error bars on each experimental point have been left out for clarity. The best fit trajectories for each of the three cylinders are shown in Figure 6 (b-d). The best fit viscosity estimates were 35, 41 and 20 Pa·s, for the 50.8, 25.4 and 12.7 μm diameter cylinders, respectively. Like in Figure 6 (a), additional trajectories have been plotted corresponding to

viscosities 0.5, 0.67, 0.8, 1.25, 1.5 and 2 times these best estimates. There are also trajectories shown for cylinder radii of ±0.25 μm from the mean to show the effect of the uncertain cylinder size. The vertical error bars shown on each experimental point represent 2.5 μm, or ~1 pixel. Horizontal error bars showing the relative timing uncertainty would be near the marker size and so are not included.

The range of estimated viscosities for the four geometries is larger than the uncertainties presented in Figure 6 account for. The model also consistently underestimates the displacement of the particles at early times, i.e. it overestimates the drag force. These two discrepancies may indicate a failure of the Newtonian model or they could be the product of imperfect analytical assumptions. For example, the initial acceleration caused by the shock-particle interaction has been neglected. Also, the assumptions of steady flow and a no-slip boundary are not well approximated by the experimental conditions. While the former is obvious from the loading conditions, evidence of the latter can be seen in Figure 3 (b) where the Au tracers disconnect from the entrained cylinders. The model itself is also highly idealized, containing none of the temperature, pressure or strain rate terms which might be necessary. Rather than pursue more cumbersome analytical models, the next section will apply direct numerical simulation toward understanding the particle trajectory, and then also the surrounding polymer flow field.

Pseudoplastic simulations

Numerical simulations provide added flexibility for modeling the polymer's shear response, making it relatively easy to explore all manner of pressure, temperature, strain rate and damage effects. However, incorporating each of these effects into a realistic constitutive model is a herculean challenge that is still ongoing for even the best studied materials. Instead, this

section aims to identify the most important phenomenology needed to match our observations of the polymer behavior. Even within that limited scope, we are left with basic questions, like whether the polymer really behaves like a fluid? While the Newtonian model produced promising agreement with the trajectory data, there is no guarantee that this is a unique result. In fact, substantial strength has previously been reported in shocked polymers [17].

A pseudoplastic model provides an intuitive way to explore this question because at one extreme it reduces to Newtonian viscosity, while at the other it becomes perfectly plastic. For intermediate cases, it can be thought of as a strain rate dependent strength or viscosity. Appealingly, a pseudoplastic model only has two critical material parameters, representing the shear resistance and the strain rate dependence. This provides a means to capture a broad range of phenomenology in simple, easily interpretable, terms. The specific form chosen was,

$$\sigma = k\left(\frac{\dot{\varepsilon}}{\dot{\varepsilon}_r}\right)^n \qquad \text{Equation 2 (a)}$$

$$k = 2\dot{\varepsilon}_r\mu \qquad \text{Equation 2 (b)}$$

where σ is the shear stress, k is the shear resistance parameter, μ is the dynamic viscosity, $\dot{\varepsilon}$ the strain rate, n is the so-called flow exponent and $\dot{\varepsilon}_r$ is a reference strain rate. Known as the Ostwald–de Waele equation, this form is commonly used to idealize shear thinning (non-Newtonian) fluids. It has been slightly modified in Equation 2 (a) by the addition of $\dot{\varepsilon}_r$. When the flow exponent is equal to 1, the model reduces to that of a Newtonian fluid with a viscosity of μ. At n = 0, it reduces to a constant shear strength of magnitude k. A reasonable initial guess for the values of μ can be made from the analytical results. The exact value of $\dot{\varepsilon}_r$ is relatively unimportant, though values close to the maximum encountered will better include the full nonlinear effects of n. After initial testing, we chose the value of $\dot{\varepsilon}_r$ to be 50 μs^{-1}.

Iterating through a range of (n, k) parameters, 176 particle trajectories were simulated for each geometry. The range of n covered 0 to 1 in steps of 0.1, and the k values were 0.10, 0.25, 0.30, 0.40, 0.50, 0.60, 0.75, 1.00, 1.25, 1.50, 2.00, 3.00, 4.00, 5.00, 6.00 and 8.00 GPa. The mean absolute deviation of these predictions from the observations was computed and plotted in Figure 7 as contour maps. This deviation (d) was calculated as,

$$d = \frac{\Sigma\left|\frac{y_{DNS}-y_{exp}}{y_{exp}}\right|}{N}, \qquad \text{Equation 3}$$

where y_{DNS} and y_{exp} are the respective displacement from the simulation and experiments, and N is the number of comparisons. The vertical axis represents n, which is the unitless strain rate sensitivity parameter from Equation 2 (a). The Horizontal axis represent the shear resistance parameter k, having units of stress (GPa). It is equally valid to consider this shear resistance in terms of μ and in units of viscosity (Pa·s). It is perhaps most intuitive to think in terms of stress when n ~ 0 and viscosity when n ~ 1, and so both labels have been applied to Figure 7. The conversion is simply that provided in Equation 2 (b). The blank white area in Figure 7 (a) represents values of (n, k) space where the simulations failed to run to completion. Fortunately, this region of phase space is likely not relevant to the study at hand.

The darkest blue regions in Figure 7 represent the cases where the model predicted trajectories that were closest to the observed ones (<5%), and each rising contour marks an additional 5% error. Consider first only the subset of these blue regions where n =1. This is the case in which the pseudoplastic model reduces to Newtonian viscosity. The values of μ which produced the lowest mean error for each map were 15, 40, 50, 25 Pa·s, which correspond to the spheres and the 50.8, 25.4, 12.7 μm diameter wires respectively. The trend in this list is the same as in the analytical drag model, where the 25.4 μm cylinder led to the highest viscosity

estimate, followed in turn by the 50.8 and 12.7 μm cylinders and lastly the 20 μm spheres. When these values were extracted without first time-averaging the errors, the result was viscosity estimates that were smaller when estimated from early times and larger when estimated from late times. This is the same trend observed in the analytical model, where the Newtonian viscosity overestimated the force at short times. The repetition of these finding for the simulations indicates that they are more likely due to the Newtonian model itself rather than the analytical assumptions. This is because the simulations naturally relax the steady flow assumption, and the boundary condition has been made more realistic. The direct numerical simulations also account for the shock-particle interaction that was neglected in the preceding section.

Looking at the whole range of (n, k) space, it will be observed that there is a crescent shaped band having low error in each map of Figure 7. Inside these regions, the error gradient is high in one direction while very low in the orthogonal one. That low error gradient makes it difficult to confidently determine a local minimum. In the case of the 50.8 μm cylinder, for any value of n from 0 to 1, there exists a k value such that the overall error remains less than 10%. The implication is that a perfectly plastic solid, a Newtonian fluid, or a pseudoplastic model could all predict the trajectory with similar accuracy. In other words, the good agreement of the analytical Newtonian fluid model with the data is not particularly convincing evidence that the polymer is fluid-like.

To resolve this question with more certainty, we will turn to the flow field within the polymer. In each simulation, bands of polymer were tracked whose initial positions corresponded to the Au films imaged in Figure 3 (b). This provides a direct comparison between the experiment and the simulation. Rather than make another exhaustive comparison though (n, k) space, it is more convenient to look at only values that accurately predict the trajectory. Six

such values were chosen and are marked by the black circles in Figure 7 (b). The 50.8 μm wire was selected for this comparison because the flow field is the largest and so easiest to resolve in the images. For each set of (n, k), the predicted flow field was extracted from the simulations at times within 12.5 ns of the experimental observations. These are overlaid in Figure 8, with the calculated tracer lines in yellow, and the radiographed Au films shown in grayscale. The simulated and experimental images were aligned using the tracer lines far from the cylinders. This reduces any small timing offsets to show the flow field differences, emphasizing the effect of the strength model over that of the equation of state. The images are shown in the same moving reference frame as in Figure 3 (b). Since the selected (n, k) values come from the low error region of Figure 7 (b), the simulated and experimental particle positions are close, though the average nature of the error in Figure 7 (b) means that the agreement is better at certain observation times than others. For values of n close to 1, the simulated flow field shows a disturbance that extends too far radially from the W cylinders. At these more viscous-like n values, the simulated tracer lines also stay too closely attached to the cylinders, rather than pulling free as seen in the experiment. This occurs despite the full-slip boundary conditions, which would be expected to promote separation. Both these discrepancies were resolved at lower values of n, where the constitutive behavior moves away from the viscous and toward constant shear strength. Judging from Figure 8, the best values of (n, k) would be close to n = 0.2, k = 0.75, or perhaps n = 0.0 and k = 0.5. Though not shown here, the simulated flow fields for the other two wire diameters led to similar conclusions. The effects of alternate simulation setups are briefly explored in the supplemental information (Appendix C), including a recalibration of these parameters in the practical case of nonconformal meshing and mixed zone advection.

Endless variations of this analysis could be performed, and incrementally better fits obtained at the cost of more free parameters in the model. With enough effort, it would be possible to perform Bayesian optimization to ensure the best possible choice of parameters for a given model, along with bounds on their uncertainty (see for example [18]). Instead of embarking on such a study, the next section will take the present simple model and see how it might be used to better understand the bulk polymer-W composite.

Application to continuum wave profiles using DNS and scaling analysis

Continuum simulations

The preceding discussion aimed to show how the shock response of isolated particles depends on the matrix's shear response but did not connect back to the motivating topic of bulk composites. To do this, fully 3D calculations were performed for comparison against recently published data on composites built from the same material system [6]. Briefly, these experiments consisted of gun driven plate impacts with continuum wave profiles recorded at a composite-LiF interface via VISAR. The experimental velocimetry traces are reproduced in Figure 9 for composites with 5 vol% and 40 vol% W filler by volume. To match these experiments, simulations were setup with 16 μm diameter particles randomly dispersed in a polymer matrix to volume fractions of 5-40 vol%, see the supplemental material (Appendix C) for more details. The simulated wave profiles, plotted in Figure 9, report the mean velocity in the polymer and W zones initially adjacent to the LiF window. The red lines in Figure 9 (a, b) show the result of a zero-strength/inviscid polymer model, i.e. the inviscid hydrodynamic case. The blue lines reflect pseudoplastic parameters of n=0.2, k =0.4 GPa. These were selected by using the n value determined from Figures 7 and 8 and then recalibrating the k value for the simulation's no-slip setup, as described in Appendix C.

The inviscid model underpredicts the acceleration for the 5 vol% W composite, while the pseudoplastic model is in better agreement with the data. The pseudoplastic model's faster approach to the steady state is because the matrix shear resistance helps to accelerate the W particles, apparently to an extent that is significant relative to the inviscid hydrodynamic effects. For the 40 vol% W composite, the pseudoplastic and inviscid models produced similar results and were both in good agreement with the experiment, with the pseudoplastic model performing slightly better. In this case, the contribution of the polymer's shear resistance was apparently small compared to wave reverberation effects. This agrees with Vogler et al.'s [19] conclusion that even an inviscid simulation can capture much of the 'apparent viscosity' in the response of a heavily particle loaded polymer. The same trends can also be seen in the simulated velocity fields shown in Figure 9 (c, d). In the 5 vol% W composite, the inviscid polymer model leads to a velocity field that is less uniform than for the pseudoplastic one. For the 40 vol% W case, the two models again lead to more similar predictions. Overall, these results indicate that the shear resistance of the matrix plays an important role at low filler volumes that diminishes as the filler fraction increases. A possible physical basis for this shift will be discussed in the next section by way of a scaling analysis.

Scaling Analysis

It remains to explain the circumstances in which the matrix shear resistance plays an important role, and when the transition to a reverberation dominated response occurs. The relative balance of these two effects can be quantified by comparing their characteristic timescales. Whichever acts over the shorter timescale will control the response because it is the one most responsible for driving the composite into equilibrium. Take the shear response to be approximated by Stokes drag because the added accuracy of the Clift-Gauvin solution is not

worth the trouble in this scaling analysis. In this case, the time constant for the particle's asymptotic approach to it steady velocity is,

$$\tau_{shear} \propto \frac{l_p^2 \rho_p}{\mu} \qquad \text{Equation 4}$$

where, l_p is the particles length scale, ρ_p is the particle density and μ is the fluid viscosity. This is the exponential time constant from the solution to the differential equation formed by substituting Stokes' law into Newton's second law. Dividing τ_{shear} by a time characteristic of the acceleration due to wave reverberation (τ_{hydro}) provides the following nondimensional number,

$$N_d = \frac{\tau_{shear}}{\tau_{hydro}}. \qquad \text{Equation 5}$$

When N_d is small, it indicates that the viscous timescale is the smaller of the two and so the shear resistance of the matrix is important. If on the other hand N_d is large, then the viscous effects are slow and can be neglected. When this occurs, it means that shock reverberation drives the composite to equilibrium before viscous drag has time to exert much effect. To get a better sense of this behavior, an expression for τ_{hydro} is needed. This has been studied for laminate composites by Chen and Gurtin [20], whose results is that,

$$\tau_{hydro} = \left(\frac{l_p}{U_p} + \frac{l_m}{U_m}\right)\left(\frac{\rho_p U_p + \rho_m U_m}{\rho_p U_p - \rho_m U_m}\right), \ \rho_p U_p > \rho_m U_m, \qquad \text{Equation 6}$$

where, ρ_m, is the matrix density, and U_m and U_p are the matrix and particle wave speeds. In applying this result to particulate composites, there is an assumption that laminate thicknesses have some equivalent length scales, which is characteristic of the interparticle spacing (l_m) and particle size (l_p). This may not be rigorously correct, but the existence of a 1D steady wave suggests that it is not wholly inappropriate. This scaling is expected to breakdown as the

interparticle spacing approaches 0 and momentum transfer shifts from wave reverberation to direct particle-particle contact. This would occur for very densely filled composites in which l_m is initially small. It could also occur for less dense cases where a large compression of the matrix reduces the spacing between the less compressible particles.

Equation 5 can now be used, at least qualitatively, to predict the effects of composition and microstructure on the relative importance of shear resistance and reverberation. An increase in the composite's fill fraction will reduce l_m, which in turn reduces τ_{hydro} and increases N_d. Remember that an increase in N_d indicates that reverberation gains in importance relative to shear. An increase in the particle size (l_p) will increase both τ_{hydro} and τ_{shear}, but the quadratic power in τ_{shear} makes that term dominate, leading to an increase in N_d. In terms of material properties, an increase in the matrix viscosity should obviously lead to a more shear dominated response.

Further analysis quantifying how composite behavior transitions between 'low' and 'high' values of N_d (Eq. 4) is ongoing. This effort should provide both numeric values for N_d and a sense of the scaling's domain. Such results would extend the utility of N_d beyond an explanatory role and allow more predictions, like determining if it is appropriate to neglect shear strength for a given composite. For the moment, the usefulness of Equation 4 is that it conceptually describes how wave propagation and shear stresses compete to shape wave profiles, and how that competition is affected by microstructure and material properties.

Conclusions

In-situ radiographs showed the momentum exchange process between a shocked polymer and W particles embedded in it. This provided a basis for comparing multiple polymer

constitutive models. While a Newtonian fluid model was successful in approximating the particle trajectories, it failed to predict the flow field within the polymer. A pseudoplastic model proved more consistent with the polymer flow field. This pseudoplastic model led to improved direct numerical simulations of the experimental wave profiles for bulk composites, especially when the volume of filler was low. These simulations showed the relative importance of shear resistance versus shock reverberation, a transition which was quantified through a scaling analysis. These inferences are underpinned by the fact that the simulations used only independently estimated material properties, instead of iterative fitting to the wave profile. A proposed nondimensional number makes it possible to estimate the relative contribution of these forces, though the precise nature of this scaling warrants further analysis.

Acknowledgements

This work was performed under the auspices of the U.S. Department of Energy by Lawrence Livermore National Laboratory under Contract DE-AC52-07NA27344. This publication is based in part upon work performed at the Dynamic Compression Sector at the Advanced Photon Source supported by the Department of Energy, National Nuclear Security Administration, under Award Number DE-NA0002442. This research used resources of the Advanced Photon Source, a U.S. Department of Energy (DOE) Office of Science User Facility operated for the DOE Office of Science by Argonne National Laboratory under Contract No. DE-AC02-06CH11357. The Video Spot Tracker software was available thanks to CISMM at UNC-CH, supported by the NIH NIBIB (NIH 5-P41-RR02170)

Figures and Captions

Figure 1: Experimental velocity traces for impact on a pure polymer (solid black) and polymer-5 vol% W composite (solid blue) under the same impact condition. The velocity history for the composite shows orders of magnitude slower acceleration than for the pure polymer. Details of this measurement are reported in Bober et al. [6].

Figure 2: (a) Schematic of the experimental setup showing the impactor arriving from the left, the polymer-W sample and the X-ray imaging direction. Detailed views of the two sample configurations are shown in third-angle orthographic projections in (b) and (c). In (b) 20 μm W spheres are arranges in a regular lattice, and in (c) three W cylinders are encased between layers of polymer and thin Au films. The uppermost projections are of the radiographic imaging direction. The vertical direction is orthogonal to the shock and x-ray directions. To help visualize the particle arrangement, alternating layers of the lattice have been color coded red and blue, which explain the stagger visible in the X-ray projection.

Figure 3: Radiographs of an array of metal spheres (a) and cylinders (b) contained in a polymer matrix undergoing shock compression. Flow in the polymer is tracked by Au films in (b). The shock wave is visible as a jump from a light to dark background and the Al buffer plate is shown by the black region at the far left. The black area in the extreme right of the fourth frame in (b) is a consequence of shifting the images to follow the buffer motion. This translation brings into the frame an area not captured by the camera, which has been colored black. The images in (a) are shown in the laboratory reference frame, while those in (b) are shifted to one fixed to the buffer. This change in reference frame make it appear that the buffer is not moving and so highlights the relative motion W wires and Au layers. The labeled times are relative to the first frame, not the events depicted.

Figure 4: An x-t diagram showing the displacement of the Al buffer and metal spheres, plotted as a function of the time elapsed since each was particle struck by the incident shock wave. In (a) the displacement is that viewed from the stationary laboratory reference frame, while in (b) the reference frame is taken to be moving at the same speed at the Al buffer (1.4 km/s).

Figure 5: An x-t diagram showing the displacement of the metal rods, tracer nanofilms and Al buffer. Like in Figure 2 (b), the reference frame has a constant velocity of 1.4 km/s. The time of the first available camera frame was set to t=0. Each observation is marked by a cross.

Figure 6: Trajectory predictions for the metal spheres (a) and cylinders (b-d) based on a Newtonian fluid model for the polymer. The best fit viscosities (solid black) are shown along with shaded bands where the best viscosity was scaled by $\times/\div$ 1.25, 1.5 and 2. Predictions bounding the uncertainty due to the measured radii are shown in dashed red. The data is shown as black dots.

Figure 7: Surfaces representing the error of trajectory predictions for the metal spheres (a) and cylinders (b-d) based on a pseudoplastic fluid model. The horizontal and vertical axis represent the two input parameters to this model. The white region in (d) is where simulation results were not available. The black circles in (b) show a sampling of (n, k) values which produced low errors were selected for further examination in Figure 8.

Figure 8: The observed flow field around the 50.8 μm wire (greyscale) can be compared to simulations using a range of pseudoplastic parameters (yellow). The measured flow field comes from the same Au layers described in Figure 3 (b).

Figure 9: Experimentally determined shock wave profiles for the polymer filled with 5 vol% (a) and 40 vol% (b) metal spheres (~16 μm diameter) are shown in black. Predictions from direct

numerical simulations using an inviscid polymer model (blue) and a pseudoplastic model (red) are also shown. Cross sections of the simulated velocity fields in the 5 vol% (c) and 40 vol% (d) composites are shown for both the inviscid and pseudoplastic polymers.

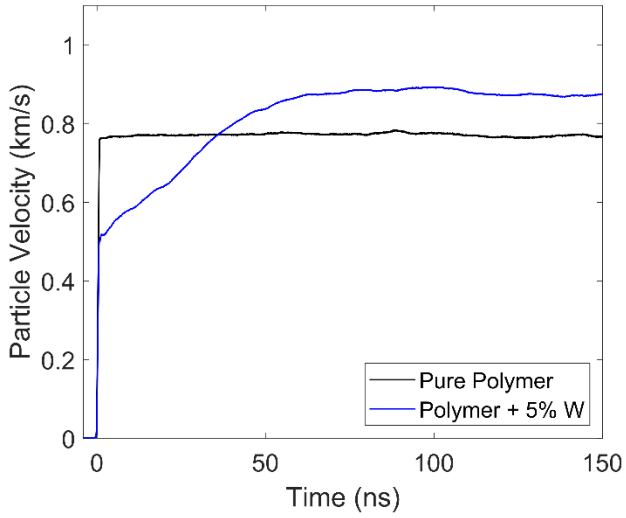

Figure 1

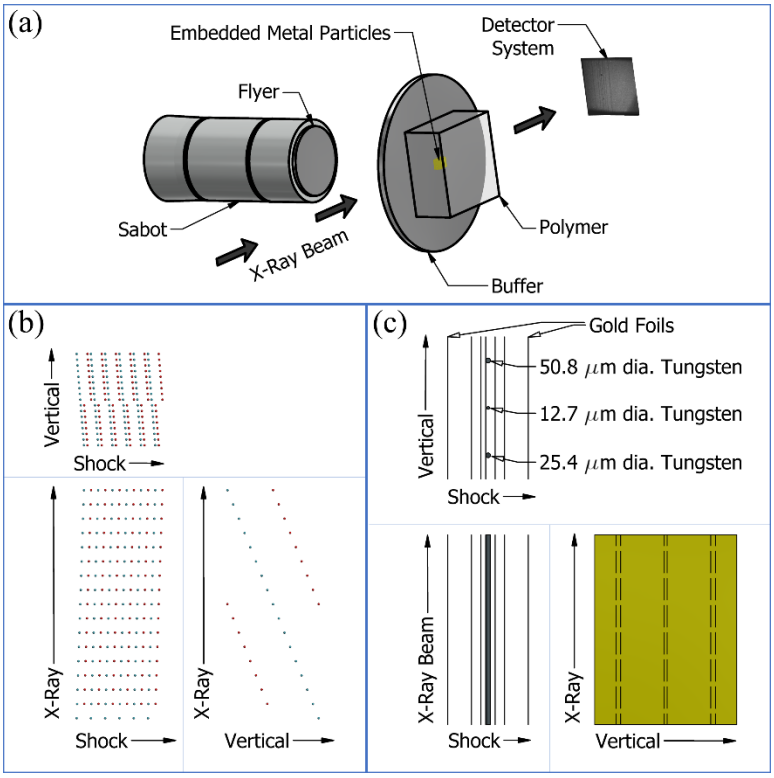

Figure 2

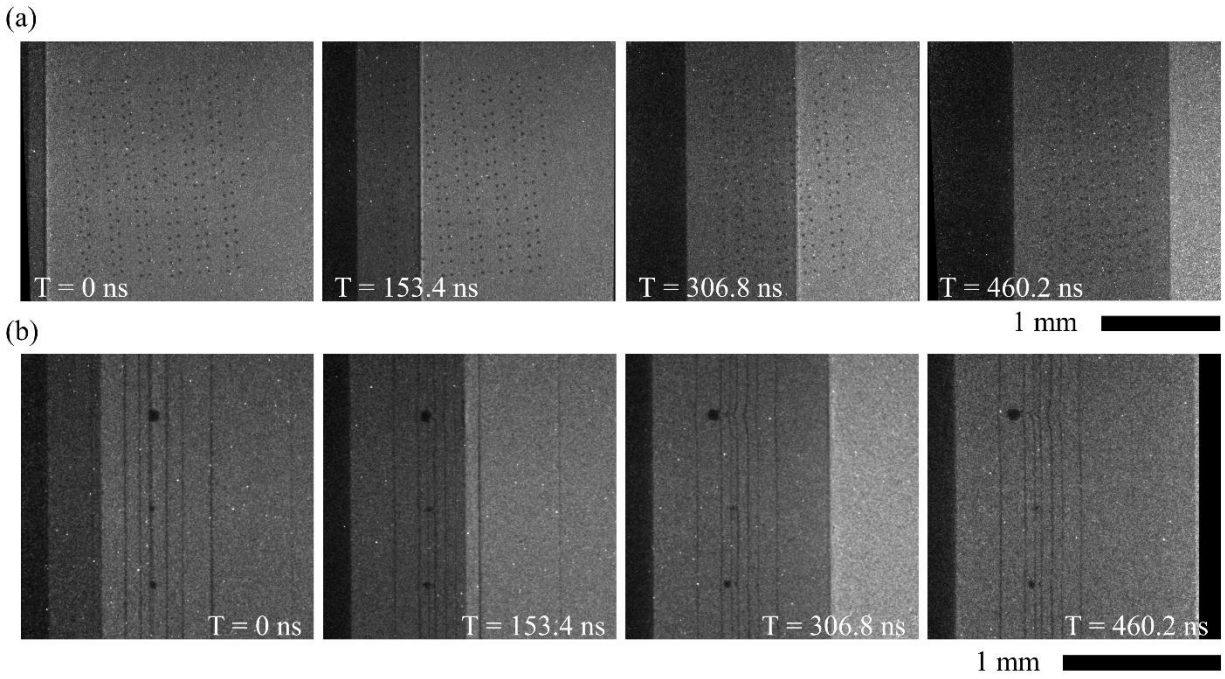

Figure 3

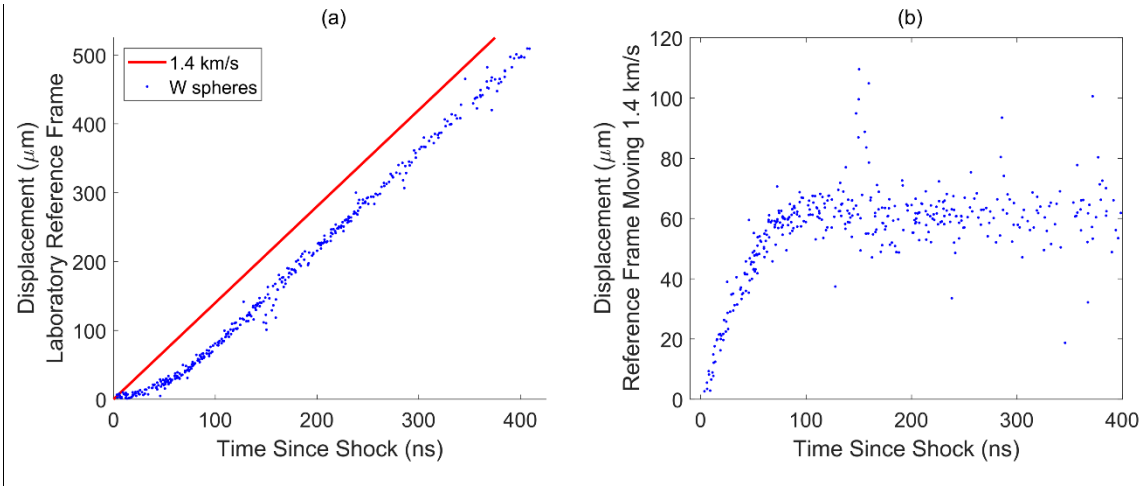

Figure 4

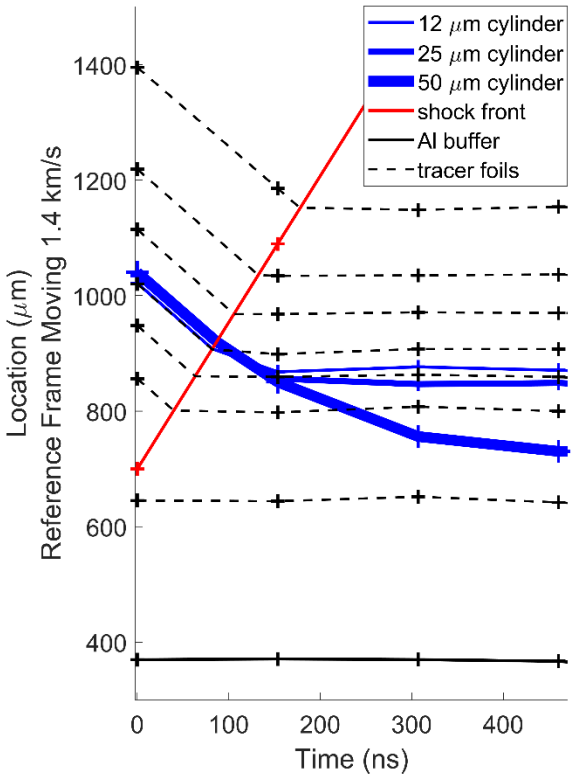
12 μm cylinder
25 μm cylinder
50 μm cylinder
shock front
Al buffer
tracer foils
Location (μm)
Reference Frame Moving 1.4 km/s
Time (ns)
1400
1200
1000
800
600
400
0
100
200
300
400

Figure 5

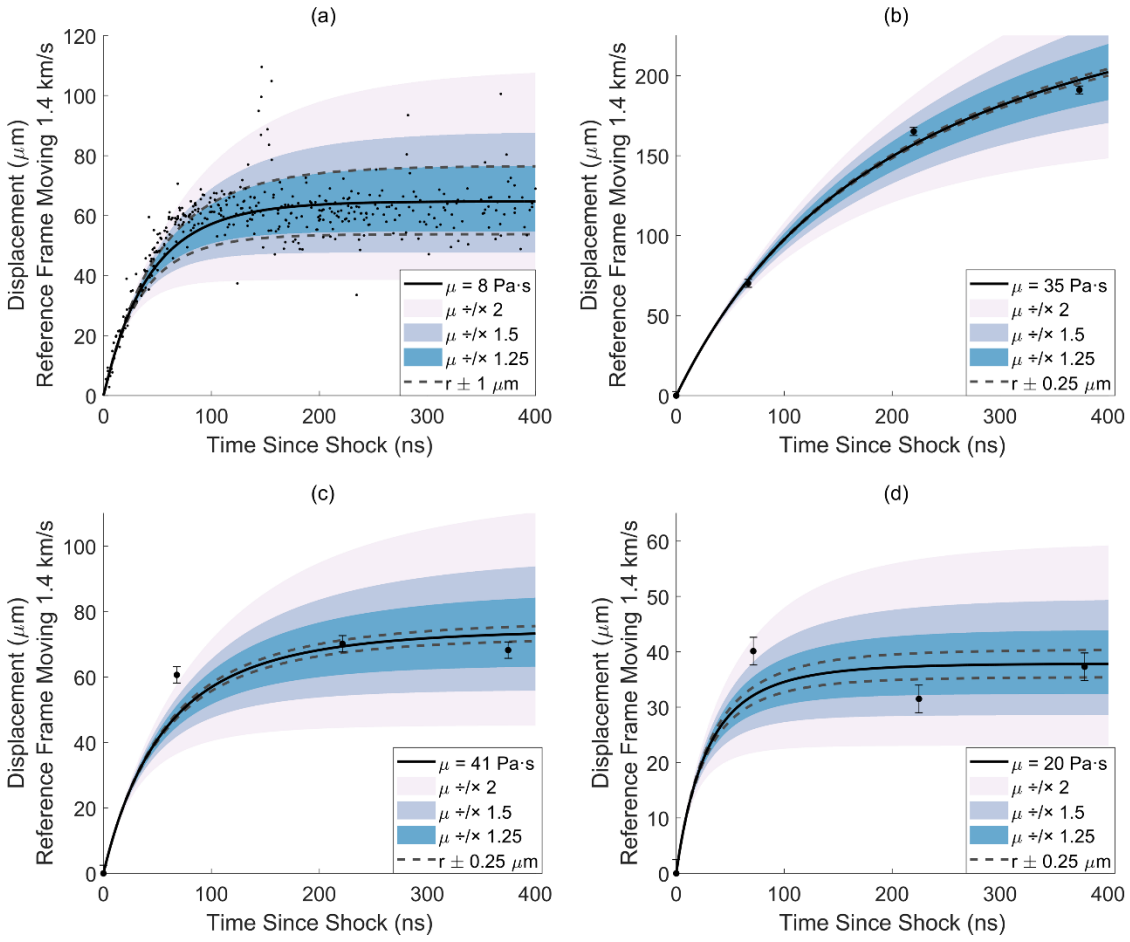
(a)
(b)
(c)
(d)
Displacement (μm)
Reference Frame Moving 1.4 km/s
Time Since Shock (ns)
μ = 8 Pa·s
μ = 35 Pa·s
μ = 41 Pa·s
μ = 20 Pa·s
μ ÷/× 2
μ ÷/× 1.5
μ ÷/× 1.25
r ± 1 μm
r ± 0.25 μm

Figure 6

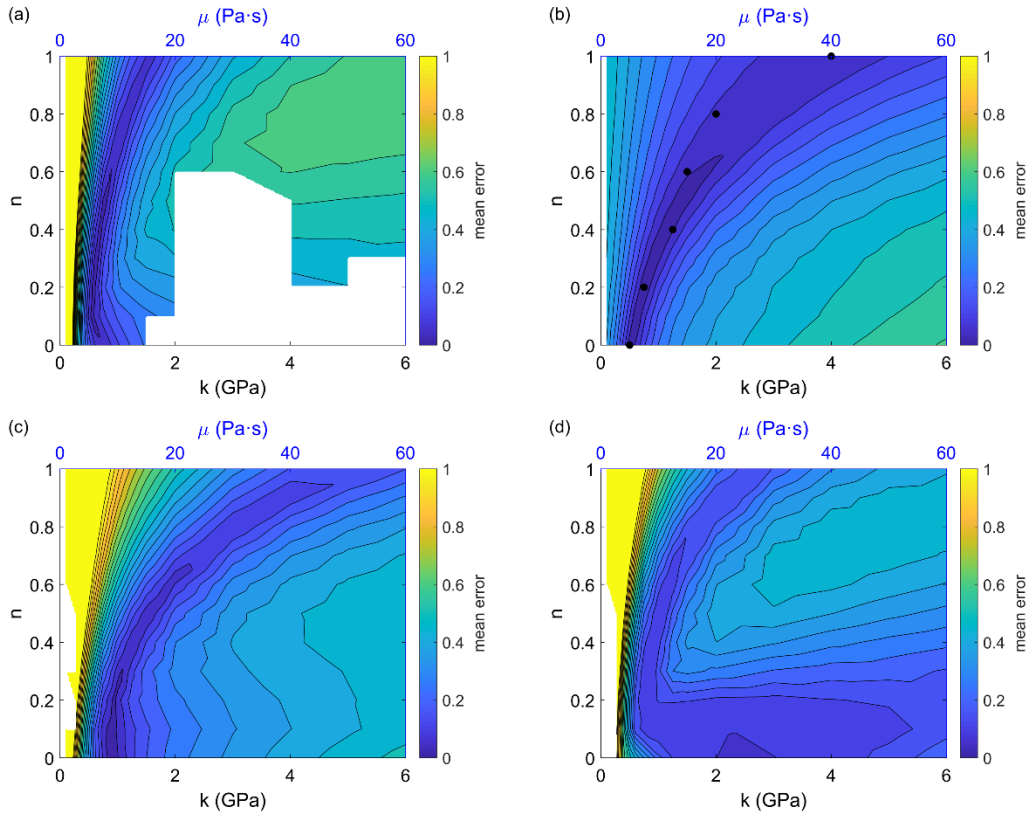

Figure 7

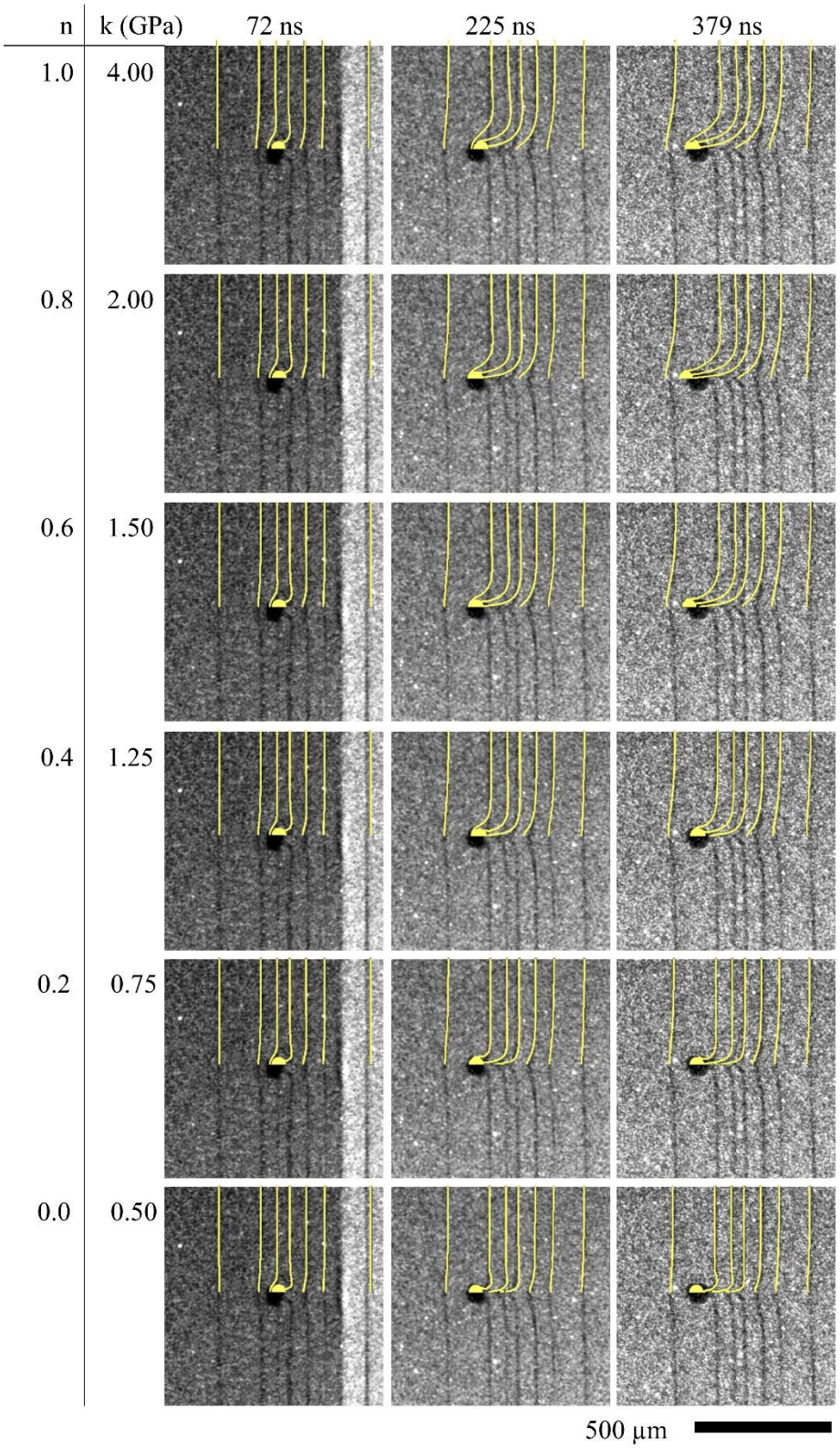
n
k (GPa)
72 ns
225 ns
379 ns
1.0
4.00
0.8
2.00
0.6
1.50
0.4
1.25
0.2
0.75
0.0
0.50
500 µm

Figure 8

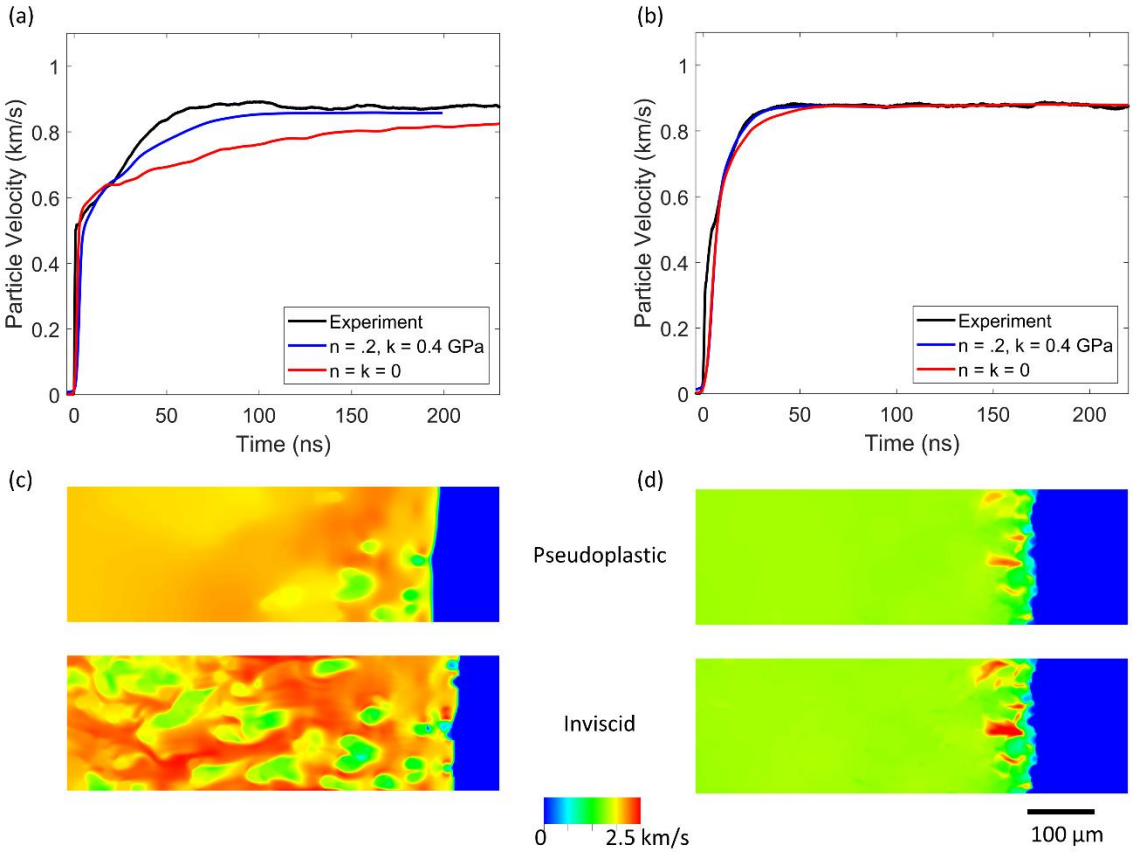
(a)
(b)
Particle Velocity (km/s)
Time (ns)
Experiment
n = .2, k = 0.4 GPa
n = k = 0
(c)
(d)
Pseudoplastic
Inviscid
0
2.5 km/s
100 µm

Figure 9

References

[1] Turneaure SJ, Sharma SM, Volz TJ, Winey JM, Gupta YM. Transformation of shock-compressed graphite to hexagonal diamond in nanoseconds, Sci. Advances 3 (2017).

[2] Barker LM, Hollenbach RE. Shock wave study of the α ⇄ ε phase transition in iron, J. Appl. Phys. 45 (1974) 4872-4887.

[3] von Neumann J. Theory of detonation waves, Progress Report to the National Defense Research Committee Div. B OSRD-549 (PB 31090) (1942).

[4] Zaretsky EB, Kanel GI. Response of copper to shock-wave loading at temperatures up to the melting point, J. Appl. Phys. 114 (2013) 11.

[5] Dattelbaum DM, Coe JD. Shock-Driven Decomposition of Polymers and Polymeric Foams, Polymers 11 (2019) 493.

[6] Bober DB, Toyoda Y, Maddox B, Herbold E, Gupta Y, Kumar K. Shock compression response of model polymer/metal composites. In: Zimmerman KB, (Ed.). Society for Experimental Mechanics, vol. 1: Springer, 2018.

[7] Rauls MB, Ravichandran G. Shock wave structure in particulate composites. in: Schonberg WP, (Ed.). Proceedings of the 2015 Hypervelocity Impact Symposium, vol. 103. Elsevier Science, Amsterdam, 2015. pp. 515-521.

[8] Setchell RE, Anderson MU, Montgomery ST. Compositional effects on the shock-compression response of alumina-filled epoxy, J. Appl. Phys. 101 (2007) 083527.

[9] Anderson MU, Cox DE, Montgomery ST, Setchell RE. Initial temperature effects on the shock compression and release properties of different alumina-filled epoxy compositions. in: Elert M, Furnish MD, Chau R, Holmes NC, Nguyen J, (Eds.). Shock Compression of Condensed Matter - 2007, Pts 1 and 2, vol. 955. Amer Inst Physics, Melville, 2007. pp. 683-686.

[10] Barker LM. A Model for Stress Wave Propagation in Composite Materials, J. Compos. Mater 5 (1971) 140-162.

[11] Jensen BJ, Luo SN, Hooks DE, Fezzaa K, Ramos KJ, Yeager JD, Kwiatkowski K, Shimada T, Dattelbaum DM. Ultrafast, high resolution, phase contrast imaging of impact response with synchrotron radiation, AIP Adv. 2 (2012) 6.

[12] Al'tshuler LV, Kanel GI, Chekin BS. New measurements of the viscosity of water behind a shock wave front, J.Exp. Ther. Phys. 45 (1977) 348.

[13] Kh. Kim G. Viscosity measurement for shock-compressed water, J Appl. Mech. Tech. Phys. 25 (1984) 692-695.

[14] Al'tschuler LV, Doronin GS, Kim GK. Viscosity of shock-compressed fluids, J. Appl. Mech. Tech. Phys. 26 (1986) 887-894.

[15] Abramson EH. Speculation on measurements of the viscosity of shocked fluid water, Shock Waves 25 (2015) 103-106.

[16] Ling Y, Haselbacher A, Balachandar S, Najjar FM, Stewart DS. Shock interaction with a deformable particle: Direct numerical simulation and point-particle modeling, J. Appl. Phys. 113 (2013) 013504.

[17] Bourne NK. On the shock response of polymers to extreme loading, J. Dyn. Behav. Mater, 2 (2016) 33-42.

[18] Walters DJ, Biswas A, Lawrence EC, Francom DC, Luscher DJ, Fredenburg DA, Moran KR, Sweeney CM, Sandberg RL, Ahrens JP, Bolme CA. Bayesian calibration of strength parameters using hydrocode simulations of symmetric impact shock experiments of Al-5083, J. Appl. Phys. 124 (2018) 205105.

[19] Vogler TJ, Alexander CS, Wise JL, Montgomery ST. Dynamic behavior of tungsten carbide and alumina filled epoxy composites, J. Appl. Phys. 107 (2010) 043520.

[20] Chen PJ, Gurtin ME. On the propagation of one-dimensional acceleration waves in laminated composites, J. Appl. Mech. 40 (1973) 1055-1060.
[21] Lind J, Jensen BJ, Kumar M. Towards in-situ high precision local material velocity measurements in lattice materials under dynamic compression. in: Chau R, Germann TC, Lane JMD, Brown EN, Eggert JH, Knudson MD, (Eds.). Shock Compression of Condensed Matter - 2017, vol. 1979. Amer Inst Physics, Melville, 2018.
[22] Michaelides E, Crowe CT, Schwarzkopf JD. Multiphase flow handbook, CRC Press, Boca Raton, 2017.
[23] Clift R, Gauvin WH. Motion of entrained particles in gas streams, Can. J. Chem. Eng. 49 (1971) 439-448.
[24] Khan AR, Richardson JF. The resistance to motion of a solid sphere in a fluid, Chem. Eng. Commun. 62 (1987) 135-150.
[25] Tritton DJ. Experiments on the flow past a circular cylinder at low Reynolds numbers, J. Fluid Mech. 6 (1959) 547-567.
[26] Huner B, Hussey RG. Cylinder drag at low Reynolds number, Phys. Fluids 20 (1977) 1211-1218.
[27] Noble C, Anderson A, Barton N, Bramwell J, Capps A, Chang M, Chou J, Dawson D, Diana E, Dunn T, Faux D, Fisher A, Greene P, Heinz I, Kanarska Y, Khairallah S, Liu B, Margraf J, Nichols A, White J. ALE3D: An Arbitrary Lagrangian-Eulerian Multi-Physics Code, 2017.
[28] Herbold E. Snowninja: A paralell monte carlo particle packing code, in preperation.

Supplemental Material

APPENDIX A: Additional Information on the materials and methods used

The samples were fabricated with a layer-by-layer addition of uncured polymer on top of previously cured material. The layers bonded seamlessly without a separate adhesive. The polymer is identical to that used in our previous work [6]. The W spheres and wires were positioned in the appropriate layer using a micromanipulator. Thin Au films were sputter coated onto the cured polymer. These Au films were limited to a 2 mm width covering the wires, which were laser cut to 2 mm in length and spaced 500 μm apart from each other. Each sample was built on a 1 mm thick plate of Al 1050, which served as the impact face and support structure. Shock waves were launched into these buffer plates by the impact of Al 6061 flyer plates moving at 1.8 km/s. The flyers were 10 mm in diameter, 5 mm thick, and mounted on 12.7 mm diameter polycarbonate sabots. They were accelerated by a single stage powder gun, with diagnostic triggering provided by a laser optical beam break.

A quasi-monochromatic X-ray beam was used for ultra-fast radiography with energy peaked at 23 keV and with an energy bandwidth of approximately 0.5% ($\Delta E/E$) given by the 2.7 cm period undulator used. The X-ray beam size at the end station used (35-ID-E) resulted in a nearly uniform intensity spot that covered the entire field-of-view (FOV) imaged by the detector system on the scintillator. The FOV imaged was approximately 2.54mm x 2.54mm. Imaging was performed by 4 separate Princeton Instruments PI-MAX4 CCD devices (1024 pixels x 1024 pixels) that are optically coupled to a thin (<100μm) Lutetium Oxyorthosilicate (LSO) scintillating screen. The LSO scintillator screen converts X-ray to visible photons which are imaged through the CCD system. A 5x Mitutoyo optical objective lens was used to focus on the

FOV resulting in an effective pixel size of 2.48 μm. Jensen et al. provides a more detailed description of the multi-frame detector system that was used [11].

Each camera had a slightly different view of the X-ray scintillator and so the resulting images were brought into coincidence via an affine transformation procedure [21]. Similar image correlation techniques were used to refine the manually estimated positions the buffer, Au films, and shock wave front. W particle positions were determined using the video spot tracking software developed by CISMM at UNC-CH (see acknowledgements section for details). While the image correlation techniques used can provide subpixel resolution, 2.5 μm (~1 pixel) will be taken as a conservative basis for the measurement uncertainty.

APPENDIX B: Newtonian fluid analysis for particle trajectories

The drag estimation becomes simpler if it is assumed that the particles are perfectly rigid and surrounded by a no-slip boundary, and that the fluid is both incompressible and undergoing steady flow. Incompressibility is justified because the speed of sound in the shocked material was 3.9 km/s, so the particles only reached 0.36 Mach in the post-shock flow. This occurred at the peak differential velocity of 1.4 km/s. Generally, Mach values less than 0.6 can be treated as incompressible [22]. The assumption of a perfectly rigid particle is supported by the small shape changes seen in Figure 3 and the expectation that a substantial flattening of the particles would be required to produce important effects [22]. The effect of the no-slip and steady flow assumptions are more approximate.

With these assumptions, a simple analytical solution for the drag exists, the exact form of which depends on the Reynolds number (Re). This nondimensional number quantifies the ratio of inertial to viscous forces and is given by,

$$Re = \frac{2\rho r v}{\mu}, \qquad \text{Equation B1}$$

where ρ is the density of the shock compressed polymer, r is the sphere's radius, v is the velocity difference between the particle and the far field polymer, and μ is the dynamic shear viscosity of the polymer. This poses a quandary because we need the viscosity to calculate Re, and vice versa. One option is to make an initial guess of the viscosity, specifically that it is so large that $Re << 1$. In this case, the drag is given by Stokes' law,

$$F = 6\pi\mu r v. \qquad \text{Equation B2}$$

A range of trajectories was calculated and the one which produced the best fit to the measurement corresponded to a viscosity of 10 Pa·s. This implies a peak Re of 4.6, which exceeds the bounds where Stokes drag is a good choice. Using this result to make a more informed guess, suppose now that the viscosity is such that the peak Re is <10. At this intermediate range of Re, the following empirical equation is typically used,

$$F = \frac{1}{2}\pi r^2 \rho v^2 C_D \qquad \text{Equation B3}$$

where, C_D is a coefficient that depends on Re. Clift and Gauvin [23] proposed that C_D be taken as,

$$C_D = \frac{24}{Re}(1 + 0.15Re^{0.687}) + \frac{0.42}{1+4.25\times10^4 Re^{-1.16}}, \qquad \text{Equation B4}$$

which has proven accurate for $Re < 3 \times 10^5$, although it is certainly not a unique choice [24]. Using this drag law, the best fit to the data was given by a viscosity of 8 Pa·s. This corresponds to a peak Re of 6.1, which is well within the valid range of the Clift-Gauvin equation. The data in Figure 6 has been shifted 3.8 ns in time relative to Figure 4 (a). This shift was determined

such that a linear fit to the earliest points passed through the origin. It is believed to represent the absolute uncertainty in setting t=0 at the time of shock-particle interaction. Abramson [15] has provided a cautionary note for this approach by pointing out that the C_D is a nonmonotonic function of Re, which introduces the possibility of misestimating the viscosity by several orders of magnitude if Re is large enough. Fortunately, the Reynolds numbers found here are small enough to avoid this problematic range.

A corresponding analysis can be conducted for the cylindrical geometries. Assuming quasi-infinite length, the drag force on a cylinder is given by,

$$F = r\rho v^2 C_{Dcyl} \qquad \text{Equation B5}$$

The drag coefficient C_{Dcyl}, was evaluated as a function of Reynolds number using the data gathered by Tritton [25]. At very low Reynolds numbers that fell below the range provided by Tritton, Lamb's approximation was used in the form provided by Huner and Hussey [26]. The drag law used in this region is relatively unimportant because the acceleration is nearly complete before the transition occurs. The assumption of quasi-infinite cylinder length is valid because the minimum aspect ratio was >40.

It is possible to better account for the dynamic nature of the experiment by incorporating added mass and Basset history force terms into the Newtonian analysis. As was pointed out by Kim [13], their inclusion relieves the need to assume steady flow conditions, which are obviously not present in the experiment. These terms are not included here because the effect is not especially large and the direct numerical simulations serve to eliminate the same assumption, while providing additional benefits like allowing particle deformation and slip boundaries.

APPENDIX C: Direct numerical simulations

DNS were performed using ALE3D, an arbitrary Lagrangian-Eulerian finite element code developed at Lawrence Livermore National Laboratory [27]. A 2D geometry was employed with axisymmetric or plane strain boundary conditions for the spherical or cylindrical geometries. Perpendicular to the shock direction, the polymer region was 15.5 times the W particle radii. The polymer length along the shock direction was effectively infinite, with shock reflection/release postponed outside the time of interest. The mesh size was approximately $1/10^{th}$ the particle diameter. Except where noted in the main text, these simulations used a conformal mesh and barred advection across the W-polymer interface.

Boundary conditions and meshing parameters were explored to learn how they might alter the estimated pseudoplastic parameters. One variation replaced the conformal mesh with a regular grid and allowed for mixed zone advection. The principal difference was to shift the value of k lower due to the non-zero surface traction. At n = 0.2, the best fit k dropped to 0.4 GPa instead of the 0.75 seen previously. The combined error map from these calculations suggested a best fit near n = 0, k = 0.3, though this result is tentative. The flow fields were also less well matched close to the rods, presumably because of the no-slip condition. While these values may be less representative of the real material properties, they are useful for simulation of the bulk composite. In those simulations, restricted interface advection and conformal meshing can be problematic and so having values tuned to capture the right physical response under the actual simulation conditions is advantageous. Increasing the W's yield strength to force a purely elastic response had little effect on the outcome. The only significantly different outcome was reached by using a conformal mesh, restricting mixed zone advection and applying a no-slip boundary condition. In that case, plastic work in the polymer at the W interface was so great that it quickly led to an unphysically large internal energy. For a realistic result under these

conditions, it is necessary to also postulate a failure mechanism to limit the shear stress in the polymer, such as a loss of shear resistance at very high temperatures.

Simulations of the bulk composite used a fully 3D geometry, with a composite volume of 200x200x1000 μm and mesh size of approximately 2 μm. The lateral boundaries for both the simulation and particle packing were set to be periodic. Particle packing accomplished using a parallel monte carlo code developed by Herbold [28]. The Al impactor, Al buffer and LiF window were included in the simulation. Unlike the 2D simulations, the W particles were not conformally meshed and mixed zone advection was allowed. For all the simulations reported, the overall volumes and mesh sizes were chosen by performing preliminary tests to determine the sizes needed to produce a reasonably converged solution.